ChemistrySelect

Research Article
doi.org/10.1002/slct.202404396

Chemistry Europe
European Chemical Societies Publishing

www.chemistryselect.org

Tunable TiO_2-Heterophase Junctions for Studying and Enhancing Photocatalytic H_2 Production Under Visible Light

Zakaria Guebli,[a] Houria Djediai,[b] Rafik Benrabaa,*[c, d] Laâldja Meddour-Boukhobza,[d] Jean François Blach,[e] Annick Rubbens,[f] Axel Löfberg,[f] and Pascal Roussel*[f]

Photocatalytic performance of titanium dioxide under visible light was optimized by preparing heterophase compounds (containing two or more phases) by hydrolysis method using $TiCl_4$ as a precursor with different concentrations (0.5, 0.7, 1, and 2) to adjust condensation modes of Ti^{4+}. The structural and textural properties of the synthesized TiO_2 multiphase were fully characterized by XRD, Raman scattering, FTIR, BET, MEB-EDX, XPS, diffuse UV–vis, and EIS spectroscopy. The increase of $TiCl_4$ amount precursor has a significant effect on the heterophase junctions of TiO_2 structure and more especially on textural and structural properties. The best specific surface area (131 m^2/g) is observed for the sample at high Ti-content (2 in Ti^{4+}). The anatase phase (79%) is detected only for 0.5 in Ti^{4+} sample. However, both rutile (R) and brookite (B) phases are present in 0.7, 1, and 2 Ti-contents. On the one hand, the band gap of 2.9 eV allows titanium dioxide to be active under visible light. In addition, the presence of rutile/brookite heterophase junction contributes significantly to the improvement of active sites for photocatalytic reaction. The separation efficiency of photogenerated electrons and holes contributes to photocatalytic evolution performance under visible light for hydrogen production. The optimal sample (0.7 content in Ti^{+4} species) which presents in its structure 52% of rutile and 46% of brookite phases presented the highest photocatalytic activity with a 230 µmol/h of hydrogen generation, attributed to the heterophase junctions R52/B46, highly pore size 20.60 nm, and relatively small bandgap energy 2.974 eV. This work opens new horizons on the creation and study of a multiphase TiO_2 that works under visible light in the fields of renewable energies and various other fields.

1. Introduction

To reduce harmful emissions and protect the environment in the face of technological developments, it is important to shift to clean energy sources. Hydrogen is a promising source of sustainable energy with a high energy density, excellent transportability, and storage capacity.[1] Unlike fossil fuels,[2,3] hydrogen has a smaller environmental footprint and can help mitigate the impact of climate change. It is possible to obtain hydrogen from natural gas, coal as a fossil resource, from water, and biomass as a renewable resource. Now, hydrocarbon fuel reformation is widely utilized as an advanced method of producing hydrogen. Nevertheless, the Industrial Revolution and the development of the world's population has increased the need for energy, resulting in excessive use of non-renewable resources like fossil fuels.[4] For the common utilization of hydrogen as a kind of energy, technological developments are needed that will enable the cost reduction of innovative sustainable hydrogen-generating methods.[5]

Researchers are developing several technologies to generate hydrogen including chemical, biological, electrolytic, photolytic, and thermochemical generation.[6,7] The production of hydrogen by photocatalysis is one of the most promising methods in this field of renewable energy. The production of energy from the photocatalysis of water means that we can use water as a source of fuel for future energy needs. Among the various catalytic materials such as WO_3,[8,9] ZnO,[10] CdS,[11] and TiO_2.[12,13] Titanium dioxide (TiO_2) is the most extensively studied, due to its strong redox ability, nontoxicity, low cost, and stable physical and chemical properties.[14,15] TiO_2 also possesses desirable electronic and optical properties that are useful in the development of photocatalysts,[16] self-cleaning materials,[17] and solar cells.[18] It finds applications in various fields including hydrogen production,[19,20] organic compound degradation,[21,22] metal ion remediation,[23,24] and organic compound synthesis.[25,26] TiO_2 exists in several crystalline forms, namely anatase, rutile, and

[a] Dr. Z. Guebli
Laboratoire des sciences et technique de l'eau et environnement, Université Mohamed Chérif Messaadia – Souk-Ahras, Souk Ahras 41000, Algérie

[b] Dr. H. Djediai
Laboratoire des Sciences, Technologie et Génie des procédés LSTGP, Faculté de Chimie, Université des Sciences et de la Technologie M-B d'Oran, B.P.1505 – EL M'naouer Oran, Oran, Algérie

[c] Prof. R. Benrabaa
Laboatoire de Physico-Chimie des Matériaux, Faculté des Sciences et de la Technologie, Université Chadli BENDJEDID El-Tarf, B.P 73, El-Tarf 36000, Algérie
E-mail: r.benrabaa@univ-eltarf.dz

[d] Prof. R. Benrabaa, Prof. L. Meddour-Boukhobza
Laboratoire de Chimie de Matériaux, Catalyse et Environnement, Faculté de Chimie, USTHB, BP32, El-Alia, 16111 Bab Ezzouar, Alger, Algérie

[e] Prof. J. François Blach
Univ. Artois, CNRS, Centrale Lille, Univ. Lille, UMR 8181, Unité de Catalyse et Chimie du Solide (UCCS), Lens F-62300, France

[f] Prof. A. Rubbens, Prof. A. Löfberg, Prof. P. Roussel
Univ. Lille, CNRS, Centrale Lille, Univ. Artois, UMR 8181 – UCCS – Unité de Catalyse et Chimie du Solide, Lille F-59000, France
E-mail: pascal.roussel@univ-lille.fr

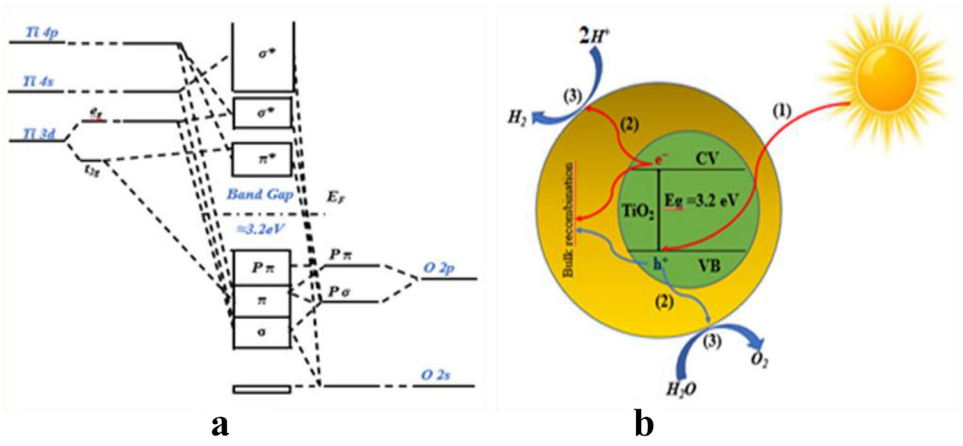

Figure 1. (a) Schematic representation of molecular orbital interactions between titanium (Ti) and oxygen (O) of TiO_2;[30] (b) Schematic representation of the important steps in photocatalytic water splitting using semiconductors.[31]

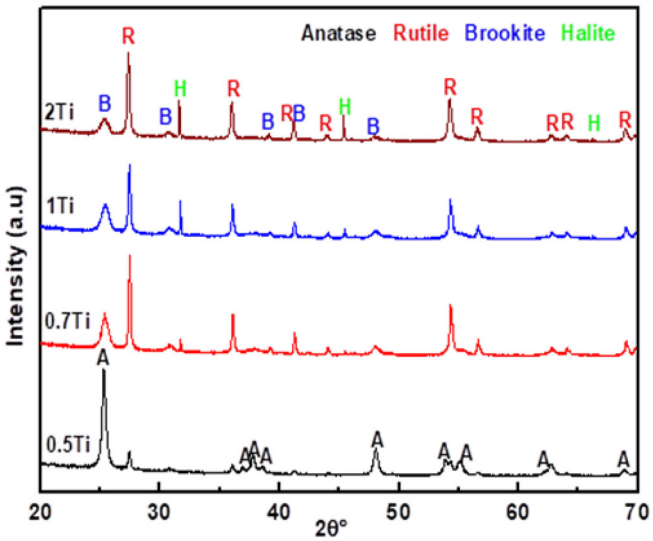

Figure 2. XRD patterns of samples (0.5Ti, 0.7Ti, 1Ti, and 2Ti) prepared with different concentrations of $TiCl_4$ precursor.

brookite, as well as another polymorph TiO_2 (B).[27,28] The unique properties of different crystalline forms of TiO_2 significantly impact its photocatalytic performance, which is dependent on the bandgap energy and kinetics of various steps involved in the photocatalytic process.[29] In Figure 1, the molecular orbital interactions between titanium (Ti) and oxygen (O) in TiO_2 are illustrated. These interactions are mainly due to the "d" orbitals of Ti and "p" orbitals of O, which contribute to the formation of bonding and antibonding orbitals.[30] Additionally, the energy difference between the highest occupied molecular orbital (i.e., valence band, VB) and the lowest unoccupied molecular orbital (i.e., conduction band, CB) is known as the bandgap energy (*Eg*). For TiO_2 anatase, the bandgap energy is approximately 3.2 eV. Figure 2 depicts the photocatalytic mechanism involved in TiO_2 water splitting, as described in.[31] The process comprises three key steps: (1) absorption of photons with a wavelength equal to or greater than the bandgap energy, leading to the creation of electron-hole pairs; (2) separation and migration of either electrons or holes from the bulk to the surface (or recombination of electron-hole pairs within the bulk material); (3) surface reactions involving photo-reduction (H^+ to H_2) and photo-oxidation (H_2O to O_2). The kinetics of these three steps play a crucial role in determining the activity of the photocatalyst. The H_2 production rate of TiO_2 is directly proportional to the number of photo-excited electrons at the water/TiO_2 interface. The determination of the overall quantum yield involves calculating the ratio between the number of H_2 molecules that evolved and the number of incident photons, as noted in.[32] For an efficient water-splitting process, the CB minimum edge of a photocatalyst should be smaller than the H^+/H_2 reduction potential (0 V vs. NHE), while the VB maximum edge must be greater than the H_2O/O_2 oxidation potential (+1.23 V vs. NHE). The water-splitting process of TiO_2 involves two half-reactions:

$$2H_2O + 4h^+ \rightarrow O_2 + 4H^+ \quad (1)$$

$$2H^+ + 2\bar{e} \rightarrow H_2 \quad (2)$$

The overall reaction can be expressed as:

$$2H_2O \rightarrow 2H_2 + O_2 \quad (3)$$

The irradiation is correlated to its intrinsic wide bandgap (3.2 eV for the anatase polymorph and 3.0 eV for the rutile one) and rapid recombination of photogenerated electron-hole pairs, which impedes its high photocatalytic efficiency.[33] For this reason, its photocatalytic performance is not sufficient for natural light utilization since the amount of UV radiation contained in solar light is too low (ca. 5%).[34] Additionally, photocatalytic water splitting is considered a "challenging reaction", with a high Gibbs free energy (ΔG° = 286 kJ mol^{-1}).[35] Therefore, many researchers are devoting their efforts to developing and synthesizing catalysts that respond to visible light. These studies include various strategies to improve the performance of titanium dioxide-based catalysts, such as the construction of porous frameworks,[36,37] surface sensitization,[38] doping,[39,40] defects,[41] or the creation of semiconductor junctions.[42,43] Among these strategies, creating semiconductor junction structures has been shown to be a successful and optimal approach that will

Table 1. Various methods for synthesizing heterophase TiO_2. A (anatase), R (rutile), B(brookite).

Precursor	Method	Heterophase TiO_2	Application	Refs.
TTIP	Hydrothermal	A-R	Methylene blue degradation	[59]
TTIP	Sol–gel	A-R	Oxalic acid degradation	[60]
$TiCl_4$	One-step condensing reflux	A-R	Rhodamine B degradation	[61]
$TiCl_3$	Hydrothermal	A-R	Hydrogen generation	[62]
TBOT	Hydrothermal	A-R	Hydrogen generation	[63]
TALH	Hydrothermal	A-B	Hydrogen generation	[64]
$TiCl_3$	Hydrothermal	A-B	Rhodamine B degradation	[65]
TiS_2	Hydrothermal	A-B	Hydrogen generation	[66]
TTIP	Sol–gel complex	A-B	Hydrogen generation	[67]
Ti $(Opr)_4$	Sol–gel complex	A-B	Hydrogen generation	[68]
$TiCl_4$	Solvothermal	R-B	Hydrogen generation	[69]
$TiCl_4$	Effective acid-regulated hydrolysis and condensation	A-R A-R-B R-B	Hydrogen generation	[70]
TTIP	LTDRP	A-R-B	Methylene blue degradation	[71]

increase the separation efficiency of photogenerated charges and holes and speed up the hydrogen generation process.[44–48] TiO_2 heterophase has been reported to be a promising strategy for improving photocatalytic performance, as it can facilitate the transfer of photogenerated electrons from one phase to another.[49,50] For instance, commercial TiO_2 "P25 Degussa" is a well-known heterophase photocatalyst, consisting of 20% rutile and 80% anatase, which exhibits excellent photocatalytic activity.[51] In addition to anatase/rutile, other TiO_2 heterophase composites, such as anatase/brookite, have been synthesized and shown to have superior photocatalytic abilities compared to pure anatase.[52,53] More recently, there has been a growing interest in developing new TiO_2 heterophase composites, including anatase/TiO_2 (B),[54,55] rutile/brookite,[56] as well as three-phase composites such as anatase/rutile/brookite,[57] and anatase/rutile/TiO_2 (B).[58] Table 1 shows the various methods used to synthesize polyphasic titanium dioxide.

The studies on Rutile/brookite photocatalyst were reported in 2008 by Di Paola et al.[72] the formulation was synthesized by thermohydrolysis of $TiCl_4$ in HCl or NaCl mediums. The photocatalytic performance was tested in 4-nitrophenol degradation and quantitative determination was performed by measuring in the UV region ($\lambda = 315$ nm). In another study, brookite/rutile was obtained using the solvothermal method. The highest phenol degradation activity was obtained from a composition of 72% brookite and 28% rutile.[73,74] Another way to prepare a controlled rutile/brookite is the hydrothermal method. The research found that the TiO_2 (38% brookite and 62% rutile[75]) sample presented the highest photocatalytic activity for RhB degradation. This explains that the biphase of brookite/rutile with optimized phase proportions is responsible for the efficient synergy effect.

In summary, TiO_2 plays a crucial role in energy and environmental fields. A major bottleneck toward developing artificial photosynthesis with TiO_2 is that it only absorbs UV light, owing to its large bandgap of 3.2 eV. If one could decrease the bandgap value of TiO_2 to the visible region, TiO_2-based photocatalysis could become and in strength a competitive clean energy source.

It is within this framework that the interest of our study falls, which aims to synthetize TiO_2 with tunable structure composition using the hydrolysis and condensation of Ti^{4+} method. During this protocol, Titanium tetrachloride ($TiCl_4$) is used as the structure precursor and NaOH as basic regulator and coordination agent to adjust the hydrolysis and condensation modes of Ti^{4+}, thereby governing heterophase junctions of TiO_2. Our findings reveal that increasing $TiCl_4$ precursor concentration significantly affects the TiO_2 structural, textural, crystal phase and heterophase junctions narrowing the band gap to 2.9 eV and enabling it to be active under visible light. Additionally, the presence of rutile/brookite heterophase junction crossing contributes to improve the active sites for photocatalytic reaction and separation efficiency of photogenerated electrons and holes, resulting in improved photocatalytic evolution performance under visible light for hydrogen production. Furthermore, the obtained sample 0.7Ti demonstrated the highest photocatalytic activity among all other samples (230 µmol/h of H_2-production) due mainly to the heterophase junctions R52/B46 leading to an improvement in the efficiency of charge separation and transfer. This study will pave the way for new research on creating and investigating multiphase TiO_2 that works under visible light for various applications, including renewable energy.

2. Experimental Section

2.1. Photocatalysts Preparation

The starting material used for preparing samples of TiO_2 heterophase is titanium tetrachloride ($TiCl_4$, Fluka 98%), which was not subjected to any further purification. At cold temperature, $TiCl_4$ was slowly added to distilled water, resulting in a highly exothermic hydrolysis reaction that produced large amounts of hydrochloric acid fumes, leading to high acidity. After continuous stirring for

Table 2. Ratios of $TiCl_4$ in water.

Samples	0.5Ti	0.7Ti	1Ti	2Ti
$TiCl_4/H_2O$ (%)	5.5	7.7	11	22

30 min, NaOH was added drop by drop, with the volume of NaOH increasing with the concentration of $TiCl_4$, until the pH of the solution reached between 2.5 and 3, leading to the precipitation of a gel. The gel was stirred again for 30 min at room temperature, then filtered and washed with distilled water and ethanol. Subsequently, the gel was dried at 80 °C for 14 h, followed by grinding and calcination at 600 °C for 2 h (Table 2).

2.2. Characterization Techniques

Powder X-ray Diffraction (PXRD) analysis was conducted employing a Bruker AXS D8 Advance-Eco diffractometer operating in Bragg-Brentano geometry, utilizing Cu Kα radiation ($\lambda = 1.5418$ Å) and equipped with a Lynx Eye detector. Patterns were systematically collected at room temperature within the $2\theta = 10$–$80°$ range, employing a 0.02° step and a 96 s counting time per step. Phase identification was performed using the EVA software.

Laser Raman Spectroscopy (LRS) was conducted at room temperature using a Horiba HR800 Raman device. The samples were subjected to a NIR Laser with a wavelength of 785 nm, and the beam was focused onto the samples using a microscopic configuration. The acquisition and data processing were carried out using LABSPEC software.

Fourier Transformed Infrared Spectroscopy (FTIR) spectra were obtained at a resolution of 2 cm^{-1} and 60 scans, covering the range of 4000 to 400 cm^{-1}. A Shimadzu 8400S model was employed for the analysis, and samples were pelletized with KBr powder (3% powder mixed with 97% KBr).

To collect diffuse reflectance data, a double-beam UV–visible spectrophotometer (Jasco V-650) equipped with an integrating sphere was utilized, covering a wavelength range of 200–900 nm. $BaSO_4$ was employed as the standard, and the powder was compacted under a pressure of 5 kbar. The diffuse reflectance spectra were used to determine the band-gap energies of the samples. This analysis involved converting the reflectance data into Kubelka–Munk function (F(R)) values.

Photoelectrochemical testing of the prepared electrodes was performed using Electrochemical Impedance Spectroscopy (EIS) on a VersaSTAT 3 galvanostat system with a three-electrode cell configuration in a 0.1 M Na_2SO_4 electrolyte. The reference electrode used was Ag/AgCl (3.5 M KCl), the platinum electrode served as the counter electrode, while the prepared TiO_2 electrodes served as working electrodes.

The specific surface area (S_{BET}) of the catalysts was determined through nitrogen adsorption at 196 °C, employing a Micromeritics ASAP2010 apparatus.

Scanning electron microscopy (SEM) and X-ray energy dispersive microanalysis (EDS) were performed on a HITACHI 4100S apparatus at 15 kV.

X-ray photoelectron spectroscopy (XPS) was carried out using an Escalab 220 XL spectrometer (vacuum generators). A monochromatic Al K_α X-ray source was utilized, and electron energies were measured in the constant analyzer energy mode. The pass energy was 100 eV for the survey of spectra and 40 eV for the single element spectra. All XPS binding energies were referenced to the C1s core level at 285 eV. The incident X-rays and the analyzer formed an angle of 58°, and photoelectrons were collected perpendicularly to the sample surface. The analysis of spectra was performed using CasaXPS software.

2.3. Photocatalytic Tests

Photocatalytic hydrogen (H_2) production was conducted within a double-walled pyrex reactor equipped with an IR cut-off filter and connected to a temperature-controlled bath to maintain a consistent temperature. The bath temperature was set to an optimal value of 50 ± 0.5 °C, a point at which water evaporation is predominant. The reactor was designed to prevent the Vortex phenomenon, and to ensure uniform dispersion of the powder (100 mg) in 100 mL of electrolytic solution (0.1 M NaOH) under moderate agitation (400 rpm) across the entire reaction space.

Prior to the photocatalytic process, the electrolytic solution was subjected to gentle agitation for homogeneity, and the system was purged with nitrogen (N_2) gas for 30 min. The photocatalytic reaction was initiated using three symmetrical LED lamps (3 × 13 W) surrounding the reactor, producing a total flux of 23 mW cm^{-2}. The generated hydrogen was subsequently analyzed using gas chromatography (Agilent Technology 7890A), and the quantity was volumetrically determined through a custom setup as detailed elsewhere.[76] The O_2 quantification was not done in this paper. Since there is no competitive reaction, the amount of evolved O_2 is easily quantified from the ratio ($H_2/O_2 = 2$).

3. Results and Discussion

3.1. Structural Properties by XRD, Raman, and FT-IR

X-ray diffraction was employed to assess the crystallinity, phase structure, and purity of the fabricated photocatalysts. The Figure 2 shows the XRD diffraction patterns of TiO_2 samples prepared and calcined at 600 °C for 2 h. In all cases, a multiphase was observed. In the sample with the lowest concentration of 0.5Ti, anatase peaks (major phase) were observed at $2\theta° = 25.28°$, 36.94°, 37.78°, 38.60°, 48.07°, 53.87°, 55.01°, and 62.70° attributed to the diffraction peaks (101), (103), (004), (112), (200), (105), (211), and (204) respectively. In addition, we notice the presence of other peaks of lower intensity at $2\theta° = 27.40°$, 36.06°, 41.23°, 44.05°, 54.33°, 56.62°, 64.08°, and 68.97° attributed to the planes (110), (101), (111), (210), (211), (220), (310), and (301) of the rutile phase, while peak appearing at $2\theta = 30.82°$ was attributed to the plane (221) of the brookite phase. For samples 0.7Ti, 1Ti, and 2Ti, no anatase phase was observed with the emergence of other peaks of rutile at $2\theta° = [62.76°, 69.78°]$ attributed to the diffraction of the planes (002) and (112) respectively. The peaks of brookite phase were observed at $2\theta = [25.38°, 30.77°, 39.19°, 42.52°,$ and $48.08°]$ attributed to the diffractions of the plans (210), (211), (204), (400), and (221), respectively. Finally, we noted that peaks of halite phase (NaCl) were also observed at $2\theta° = [31.64°, 45.37°,$ and $66.21°]$ attributed to the diffractions of the plans (200), (220), and (400), respectively. The intensity of the halite phase peaks increases with increasing initial concentration of $TiCl_4$ precursor. It was formed from the reaction of the Na^+ from the coprecipitating agent with the Cl^- from the $TiCl_4$ precursor. This may be due to the fact that the washing process was not complete. A

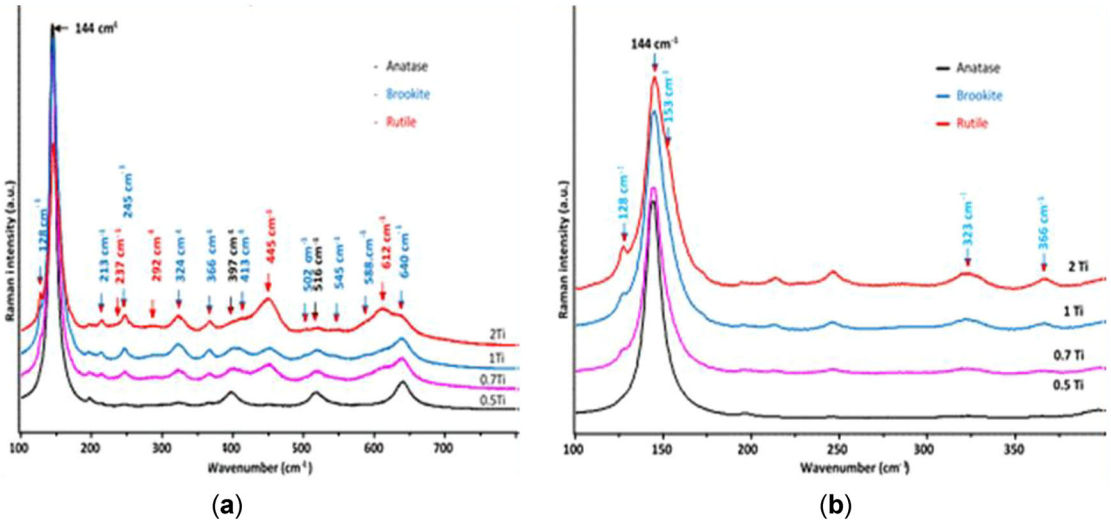

Figure 3. (a) Raman spectra of multiphase TiO_2 samples (0.5Ti, 0.7Ti, 1Ti, and 2Ti). (b) Raman spectra of multiphaseTiO_2 samples (0.5Ti, 0.7Ti, 1Ti, and 2Ti) in the spectral range: 100–400 cm^{-1}.

Table 3. The ratio of phases in each sample using the Rietveld method.

Samples	0.5Ti	0.7Ti	1Ti	2Ti
Anatase%	79	0,00	0,00	0,00
Rutile%	13	52	44	58
Brookite%	8	46	53	34
Halite%	0,00	2	3	8

comparison of XRD patterns of the samples reveals that a good crystallization of the anatase phase was obtained in the sample with the lowest concentration 0.5Ti. While the increase in the initial concentration of $TiCl_4$ precursor leads to the complete conversion of the anatase phase into rutile and brookite with good crystallization. The Rietveld refinement method was used to find out the percentage of phases in each sample (see Table 3).

Figure 3a shows the Raman spectra recorded from 100 to 800 cm^{-1} for the four TiO_2 samples, with no observed lines for higher wavenumbers. The anatase Raman spectrum presents four main bands: a very intense line at 144 cm^{-1}, in the very low frequency range, and a triplet of much weaker intensity than the first one at wavenumbers 397, 516, and 640 cm^{-1}.[77] For the rutile form of TiO_2, three bands are observed, two of equivalent intensity at values 445 and 612 cm^{-1}, and a large broad band of lower intensity at 237 cm^{-1}.[77] The brookite phase has its vibration bands largely overlap with those of the two previous forms of TiO_2. Its identification will nevertheless be possible with the vibrations located at 128, 324, and 366 cm^{-1}, a detailed study on a single crystal of brookite.[78] reinforcing this choice and assignment. For the 0.5 Ti composition, the anatase form is largely in the majority in the mixture (Figure 3a), the position in wavenumber of the weak peaks observed for this composition suggests the formation of a very small proportion of rutile (445 and 612 cm^{-1}) and brookite (245, 324, and 366 cm^{-1}). The large quantity of anatase in the mixture does not allow us to observe the line at 128 cm^{-1} located in the foot of the intense band at 144 cm^{-1}. By increasing the additional titanium content, the characteristic bands of the anatase form decrease in intensity, while those relating to the brookite phase increase in intensity as do those of rutile TiO_2 at 445 and 612 cm^{-1}. This clearly indicates the transformation of anatase into brookite and rutile by increasing the additional titanium content. If the line at 640 cm^{-1} characterizing anatase does not decrease in intensity like the two others at 397 and 516 cm^{-1}, this is due to its overlap with the line at 640 cm^{-1} of brookite form of which its concentration increases in the mixture. The feature study of intense line at 144 cm^{-1} of the anatase phase (Figure 3b) supports our writings. Indeed, we can notice the increase in the intensity of the line located at 128 cm^{-1}, a widening of the line at 144 cm^{-1} with a shift of its extremum towards high wavenumbers, resulting from the formation of the component at 153 cm^{-1} of the brookite phase increasing in intensity with the addition of the precursor. These results are in agreement with various works in the literature on titanium oxide.[79,80] Raman scattering analysis confirms the results obtained by XRD. The phase change (anatase–rutile–brookite) is proportional to the additional addition of the precursor $TiCl_4$ for the synthesis of TiO_2.

Table 4 represents the wavenumbers observed by Raman scattering for our mixed TiO_2 samples and compared them to the results of the literature.

FT-IR spectroscopy was used to study the nature of chemical bonding and identify the functional groups present in the nanostructures of multiphase TiO_2 samples. Figure 4 shows the recordings made from 400 to 4000 cm^{-1} on samples pelleted in potassium bromide. For the 420-–750 cm^{-1} range, the change in spectral feature is linked to variations in the concentration of the different phases of TiO_2 depending on the additional titanium content. However, very weak peaks appear for higher wavenumbers. It can be noted that the absorption at 3745 cm^{-1} is due to the stretching of the OH bond of the water molecule

Table 4. Raman active optical phonon modes of anatase, rutile and brookite TiO_2 species comparison with the Raman wavenumbers of synthesized polyphase titanium dioxide samples.

TiO_2 Anatase		TiO_2 Rutile		TiO_2 Brookite	
Raman Shifts of Our Samples (cm^{-1})	Published Data (cm^{-1})[77,79,80]	Raman Shifts of Our Samples (cm^{-1})	Published Data (cm^{-1})[77,80,81]	Raman Shifts of Our Samples (cm^{-1})	Published Data (cm^{-1})[78,80]
				128	125
144	144	142	145	153	152
196	196			213	194
		237	232	245	246
				323	324
				366	366
397	394				
				413	412
		445	448	502	492
516	516				
				545	545
				588	584
		612	613		
640	638			640	640
			826		

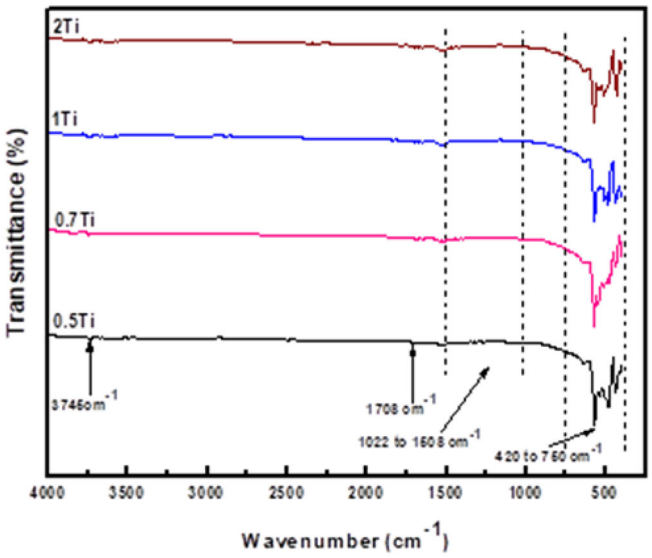

Figure 4. FTIR spectra of heterophases TiO_2 samples.

on the surface. The vibrations at 1022, 1508 cm^{-1} can be due to the residual carbonate, the band at 1708 cm^{-1} indicating the formation of carbon dioxide at the surface. These observations are in agreement with a nanometric size of the crystallites.

3.2. Textural Properties by SEM-EDX, BET, and XPS

The size, shape, and surface morphology of the samples of TiO_2 multiphase 0.5Ti, 0.7Ti, 1Ti, and 2Ti were studied using SEM with different magnifications and represented in Figure 5. 200x magnification in all samples shows scattered solid particles from

Table 5. Tabulated TiO_2 (0.7Ti and 2Ti samples) elemental composition.

	C	O	Na	Cl	Ti
0.7Ti600 - 10 kV - x900	0.87	34.05	0.93	0.62	63.52
2Ti600 - 10 kV - x900	0.64	31.65	1.26	0.91	65.54

the nodules of various sizes, while 2000x magnification shows clear, smooth particles in all samples. The particles in 0.5Ti, 1Ti, and 2Ti samples show regular shapes and large sizes. In comparison, 0.7Ti sample consists of smaller particles with different shapes and displays a relatively better distribution. Smaller particle size creates more points of interaction. It is useful for photocatalysis.[82] Figure 6 and Table 5 represent the TiO_2 (0.7Ti and 2Ti) sample's energy dispersive X-ray (EDX) spectroscopy results. The effective synthesis of TiO_2 (0.7Ti and 2Ti) samples, which mostly contain titanium and oxygen as predicted at a higher energy level, was demonstrated by EDX analysis.[83] It also indicates the presence of Cl, due to the NaCl, more visible in sample 2Ti (the presence of the carbon element is attributed to the carbon coating before the sample characterization).

Nitrogen adsorption isotherms on TiO_2 nanoparticles for the four samples were examined at incremental relative pressures to analyze and ascertain the BET surface area, pore size, and pore volume. The corresponding values for BET surface area, pore size, and pore volume of the four samples are presented in Table 6. From Figure 7, the Linear Isotherm plot of TiO_2 nanoparticles for the four samples show a stepwise adsorption-desorption branch at a wide range of pressure (P/Po): Type IV isotherm classification that is attributed to the presence of mesopores (2–50 nm), according to the International Union of Pure and Applied Chemistry (IUPAC) classification.[84] We observed an adsorbed quantity

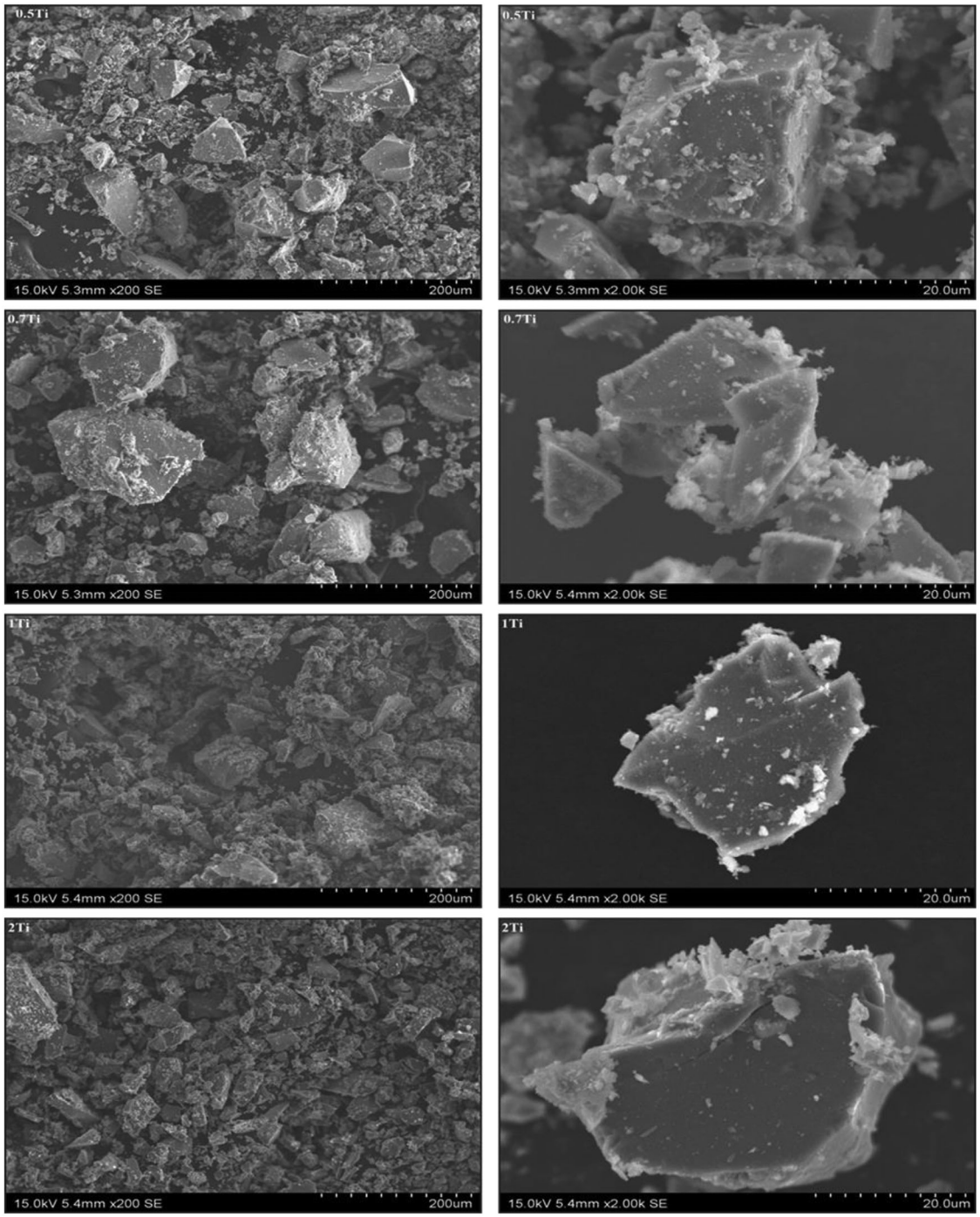

Figure 5. SEM images of 0.5Ti, 0.7Ti, 1Ti, and 2Ti samples.

Table 6. BET surface area, pore size, and pore volume of 0.5Ti, 0.7Ti, 1Ti, and 2Ti.

Samples	BET Surface Area (m^2/g)	Pore Size (nm)	Pore Volume (cm^3/g)
0.5Ti	41	11.52	0.12
0.7Ti	30	20.60	0.15
1Ti	28	16.47	0.11
2Ti	131	7.14	0.23

affinity for samples with low concentrations of 0.5Ti, 0.7Ti, and 1Ti being 76.86 cm^3/g STP 99.64 cm^3/g STP, and 75.33 cm^3/g STP, respectively. In the contrast, the sample with the highest concentration (2Ti), the adsorbed quantity increases being 151.42 cm^3/g STP. This is due to the BET surface area affinity for samples with low concentrations of 0.5Ti, 0.7Ti, and 1Ti being 41 m^2/g; 30 m^2/g, and 28 m^2/g, respectively. In the sample with the highest content (2Ti), the BET surface area is 131 m^2/g. The pore size calculated using the Barrett–Joyner–Halenda (BJH) model are 11.52, 20.60, 16.47, and 7.14 nm for 0.5Ti, 0.7Ti, 1Ti, and 2Ti, respectively. The

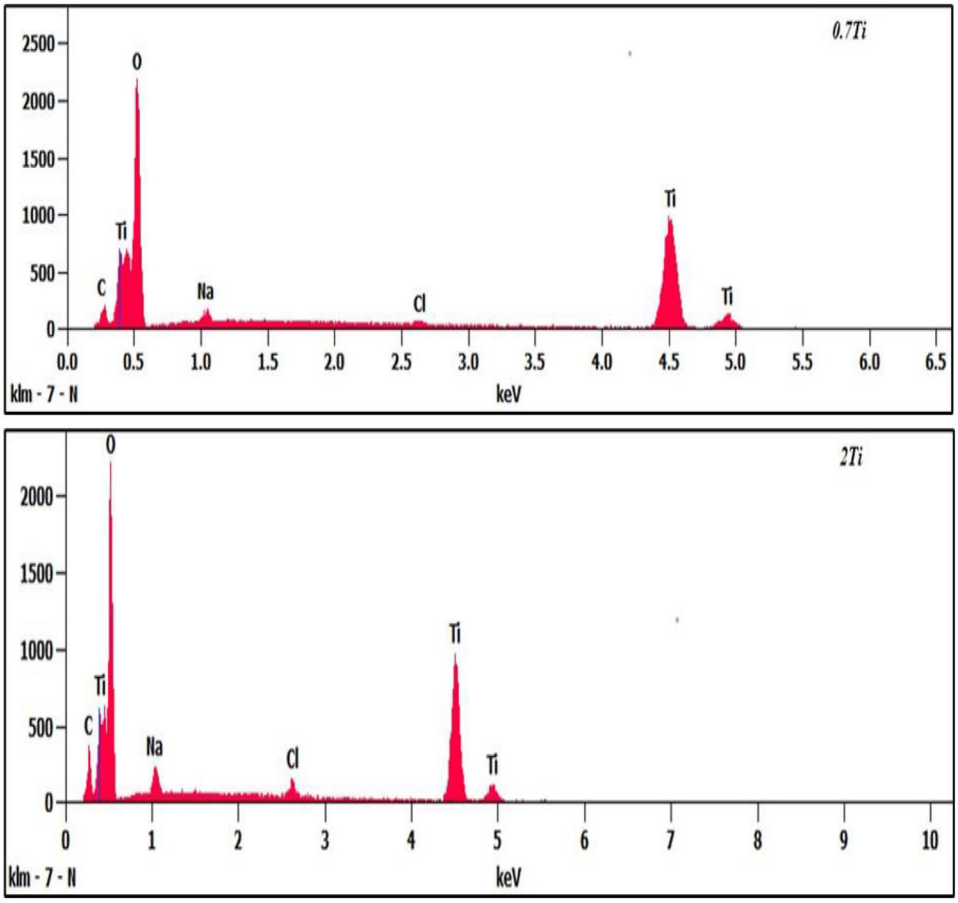

Figure 6. EDX spectra of 0.7Ti and 2Ti samples.

Table 7. The values of valence band conduction band and band gap energy for all samples.

Samples	0.5Ti	0.7Ti	1Ti	2Ti
Valence band (eV)	2.22	2.116	2.116	2.116
Conduction band (eV)	−0.76	−0.858	−0.86	−0.868
Bandgap energies (E_g) (eV)	2.98	2.974	2.976	2.984

augmentation in specific surface area can be attributed to a reduction in the crystal size of the nanoparticles.[85] Thus, it is clear that the increasing titanium concentration significantly affects the surface area of the photocatalysts. This is due to the change in the ratio of the phases of rutile, anatase, and brookite, as pointed out from the analysis of XRD and RAMAN (Table 7).

The XPS method was used to analyze the chemical composition of TiO_2 samples (Figures 8 and 9). The results showed that all samples were made up of Ti and O species. The Ti*2p* spectrum in all samples had two binding energy values, 458.4 – 458.7 eV and 464.2 – 464.5 eV, which corresponded to Ti^{4+} in TiO_2. The calculated difference in bonding energy (BE) of Ti $2p_{3/2}$ and Ti $2p_{1/2}$ (ΔBE = BE Ti $2p_{3/2}$ – Ti $2p_{1/2}$) was equal to ~5.7 eV, indicating the presence of typical Ti^{4+}–O bonds in TiO_2.[86,87] The O*1s* spectrum had two peaks, with the peak at 529.7 –529.9 eV being attributed to lattice oxygen (O_L) of TiO_2, and the shoulder peak at 531.3 eV being assigned to O_{OH} (Figure 9).

3.3. Optical Properties by UV–vis Spectroscopy

The optical properties of the as-prepared TiO_2 samples were explored through diffuse UV–visible spectroscopy, and the findings are illustrated in Figure 10a–c. All samples show high convergence in the visible light and ultraviolet light absorption region whereas the drawing shows band edge absorption around 420 nm. However, the absorption behavior of the 0.5Ti sample is different from the others, where the absorption values decrease in 0.7Ti;1Ti, and 2Ti samples until they reach a minimum of -0.5 (au) in 2Ti sample at 420 nm. This negative value indicates that the samples are transmitting more light than it is absorbing. This behavior is known as a negative absorption or a gain spectrum and can be observed in some materials with specific properties, such as doped semiconductors, quantum dots, or gain media. In this case, the presence of halite, a sodium chloride mineral (NaCl), in these three samples may be responsible for this effect. The sodium ions in halite can act as electron donors, increasing the number of free electrons in the TiO_2 and creating a gain spectrum.

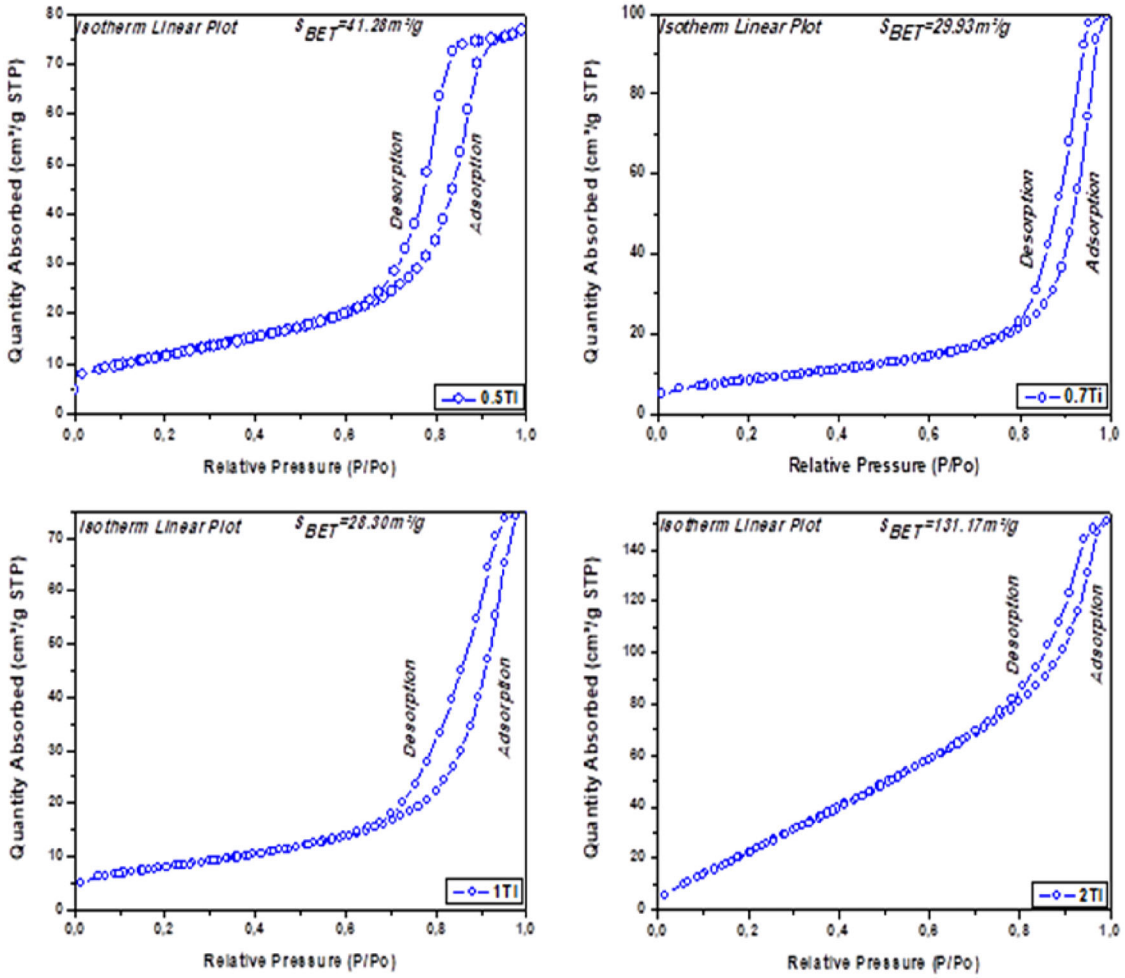

Figure 7. Plots of adsorption and desorption isotherms of the TiO_2 samples 0.5Ti, 0.7Ti, 1Ti, and 2Ti.

As shown in Figure 10b, all TiO_2 samples present a significant reflectance rate in the UV range and a fraction in the visible range, generally due to the charge transfer of the valence band (which mainly consists of 2p orbitals of oxide anions) to the conduction band (Which mainly consists of 3D t2g orbitals of Ti^{4+} cations.[88]

The band gap energy was determined using the Tauc plot method. This analysis included converting the reflection data into Kubelka–Munk function values according to the following equation (Equation 4):

$$F(R) = \frac{(1-R)^2}{2R} = \frac{K}{S} \tag{4}$$

where S is the scattering coefficient and K is and the absorption coefficient; and it is well known that the band gap is related to the optical absorption coefficient α by the Tauc function, as given by equation (Equation 5):

$$(\alpha h\upsilon)^{\frac{1}{n}} = C\left(h\upsilon - E_g\right) \tag{5}$$

where, C is a constant, $h\nu$ is photon energy, E_g is the allowed energy gap and n is a constant that depends on the nature of optical transition, $n = 2$ and 1/2 represent the indirect and direct transition, respectively. The following equation (Equation 6) can be used for a perfectly diffuse scattering compound:

$$(F(R)\,h\upsilon)^{\frac{1}{n}} = C\left(h\upsilon - E_g\right) \tag{6}$$

where in general, the band-gap energies (E_g) of the samples were calculated by plotting $(F(R)h\nu)^{1/n}$ against the photon energy ($h\nu$) and extrapolating the linear region of the curve to the x-axis.

The results are shown in Figure 10c, where a large convergence in the value of the bandgap energy for all samples is observed. The transformed Kubelka–Munk function plotted against the energy of light (Figure 10c) yielded band-gap energies of 2.98, 2.974, 2.976, and 2.984 eV for the 0.5Ti, 0.7Ti, 1Ti, and 2Ti samples, respectively. It is a typical value for mixed phase titanium dioxide. The energy band structure of the prepared photocatalysts was investigated using valence band X-ray photoelectron spectroscopy (XPS) spectrum. As depicted in Figure 11a, the linear extrapolation on the front edges of the valence band (VB) XPS spectra was employed for analysis,[70,86,89] the 0.5Ti, 0.7Ti, 1Ti, and 2Ti possess valence band positions of 2.22, 2.116, 2.116, and 2.116 eV, respectively versus normal hydrogen electrode (NHE). Thus, the conduction band position can be calculated using the relationship:

Eg = CB-VB → CB = VB + Eg to be -0.76, -0.858, -0.86, and -0.868 eV, respectively.

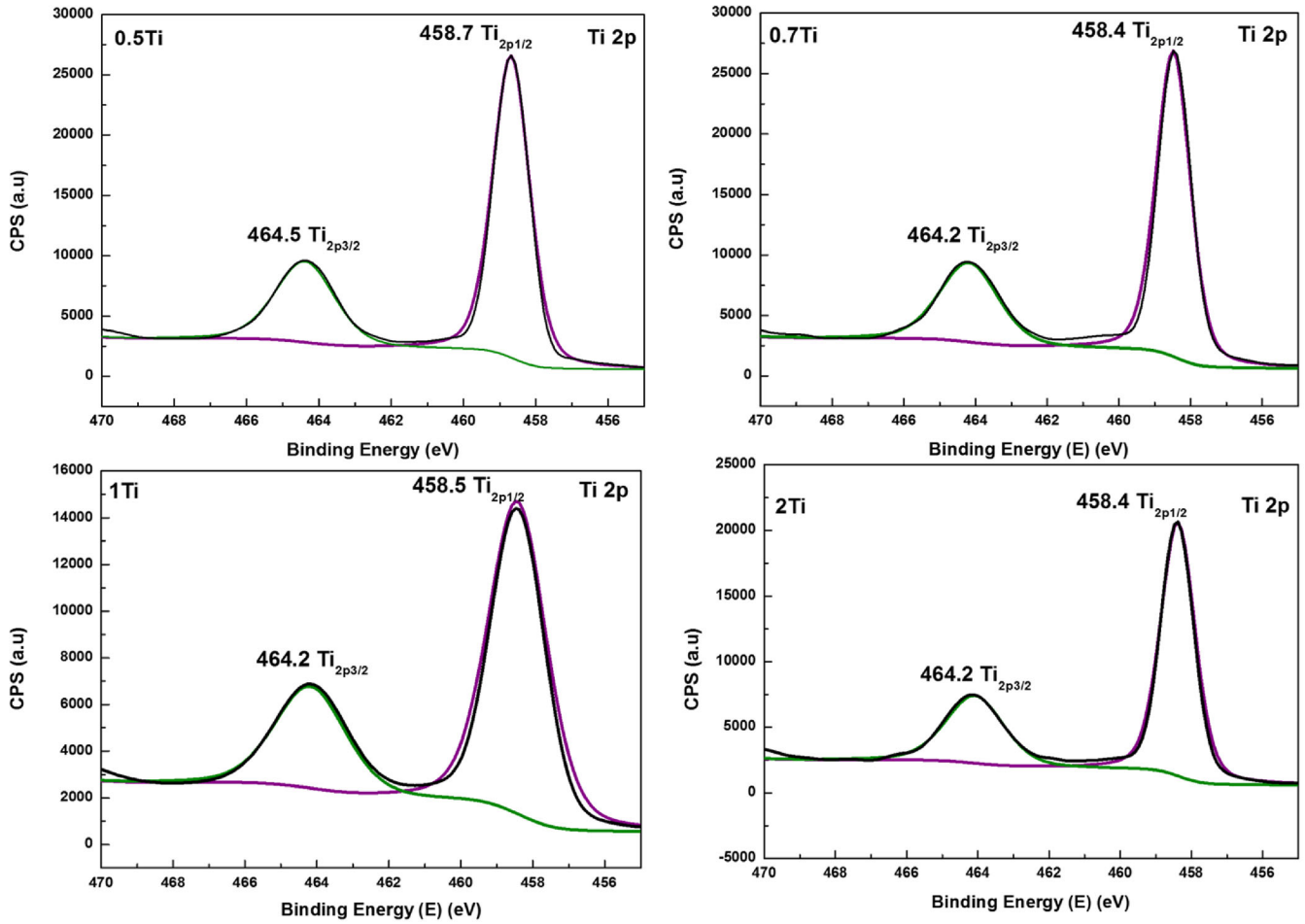

Figure 8. XPS spectra of Ti*2p* species of 0.5Ti, 0.7Ti, 1Ti, and 2Ti calcined at 600 °C.

Figure 11b illustrates the band diagrams for both the reference TiO_2 and 0.7Ti in detail. The valence band, the conduction band, and the band-gap energies are significantly higher in reference TiO_2[90] compared to 0.7Ti.

3.4. Electrochemical and Photoelectrochemical Properties

EIS studies, spanning a frequency range of 100–0.1 Hz, were conducted to evaluate the charge transfer mechanism occurring on the photocatalyst surface and predict the evolution of H_2 under radiation. EIS analysis of the 0.7Ti and 2Ti samples was performed both in the dark and under irradiation (Figure 12). The Nyquist diagram for the 0.7Ti and 2Ti samples is shown, depicting their behavior in both conditions. Semicircles observed at high and low frequencies are associated with interfacial charge transfer.

It was observed that the diameter of these semicircles decreased when exposed to radiation, indicating rapid transfer of surface charge at the semiconductor/electrolyte interface and efficient separation of photogenerated electron-hole pairs (e^-/h^+). Thus, an efficient charge transfer channel is created through the fastest intercalation/separation process, which is associated with the porous structure and high specific surface area. This observation was further supported by SEM and BET analysis. Therefore, the semiconductivity of the multiphase TiO_2 samples is confirmed, which is highly desirable in the photocatalytic process.[91]

The EIS Nyquist plot of the 2Ti($R_{58}B_{34}$) sample exhibited the smallest arc radius (Figure 12), implying the lowest charge transfer interfacial resistance. The 2Ti($R_{58}B_{34}$) sample demonstrated high and stable photocurrent intensity, indicating that the rutile/brookite phase junction effectively obstructs the recombination of photogenerated electrons and holes. From the above analysis, it can be concluded that the rutile/brookite heterophase junction endows TiO_2 photocatalyst with excellent photogenerated carrier separation ability, significantly contributing to improving the performance of photocatalytic H_2 evolution.[68]

3.5. Photocatalytic Properties in H_2 Production

The evolution of photocatalytic properties in H_2 production of the samples is presented in Figure 13a,b. Figure 13a. shows the evolution of hydrogen over time for all samples. Among these samples, 0.7Ti formulation exhibits the highest hydrogen evolution rate (230 µmol/h), compared to 0.5Ti sample, which contains the largest percentage of anatase and is free of halite, and

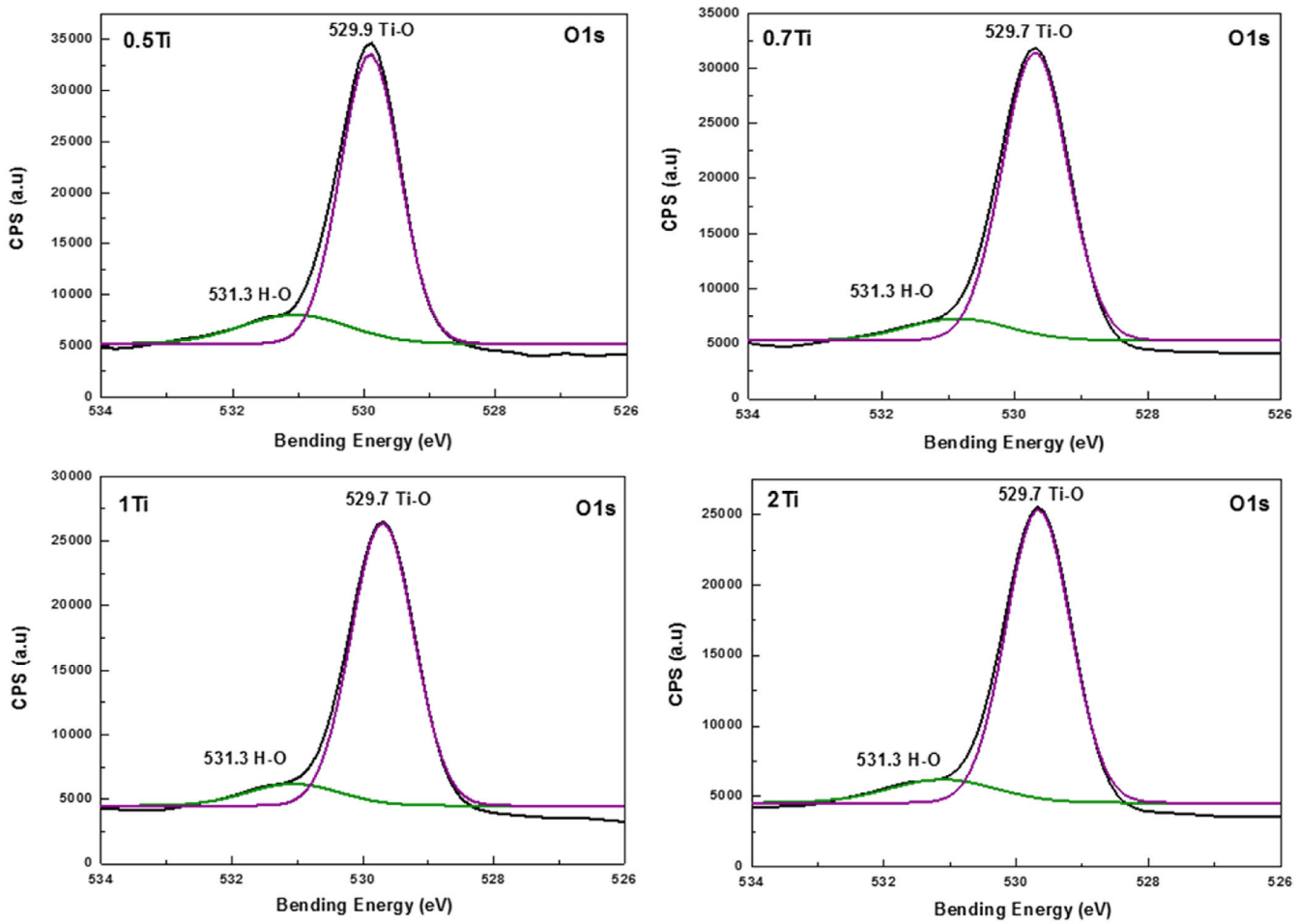

Figure 9. XPS spectra of O*1s* species of 0.5Ti, 0.7Ti, 1Ti, and 2Ti calcined at 600 °C.

has a hydrogen evolution rate of 125 μmol/h. This difference in hydrogen evolution rates may be due to the positive effect of heterophase junctions rate rutile/brookite. Sample 1Ti contains a greater proportion of brookite than rutile (Table 3), and although it has an almost equal bandgap (*Eg*) value to 0.7Ti sample (1Ti; *Eg* = 2.976 eV) (0.7Ti; Eg = 2.974 eV) and a similar surface area about 28 m^2/g, it has a lower hydrogen evolution rate of 116 μmol/h (about 43.75% lower than sample 0.7Ti). This difference in hydrogen evolution rates may be due to the proportion of rutile in the rutile/brookite heterophase junction being greater than that of brookite, which provides the photocatalyst with excellent photo-generated carrier separation ability, significantly enhancing the efficiency of photocatalytic H_2 evolution. The sample at a higher content of Ti^{4+} species (2Ti) has the lowest hydrogen production rate, despite having a high surface area of 131 m^2/g (Table 6) and the smallest pore size of 7 nm. Although it contains rutile/brookite heterophase junction and has a bandgap (*Eg*) value of 2.984 eV, the hydrogen production rate is weaker than that of the other samples, which may be due to the high proportion of halite in the sample. The halite could have played a role in inhibiting photocatalysis. In addition, we carried out a stability test after 48 h for the 0.7Ti sample to evaluate its photostability. Figure 13b shows that there was no significant decrease in the amount of hydrogen produced. The amount of hydrogen after 48 h was 219 μmol, which is approximately 95.21% of the first amount, indicating the excellent stability of 0.7Ti sample.

In summary, TiO_2 heterophase as rutile/brookite exhibits better photocatalytic activity than TiO_2 with A/R/B and B/R phases. The heightened activity can be attributed to the interaction between the two phases, mitigating recombination. The mixed phase incorporates an interfacial electron trapping site, a phenomenon documented in the literature.[92,93] The redox process can be accelerated when TiO_2 is in the mixed phase[94] resulting in a decrease in the recombination rate, an increase in luminous efficiency, and activation of the energy bandgap by light with energies lower than UV.[95] At semiconductor heterojunctions, the energy bands of two different materials come together, leading to an interaction and the band structures align close to the interface due to the discontinuous band structures of the semiconductors.[96,93] In the research by Sun.et al.[68] and Chen et al.[56] found that the valence band energy and conduction band energy are higher in the brookite phase than in the rutile phase when there is contact. Electrons move to the rutile due to the lower conduction band minimum energy, while holes move to the brookite due to the higher valence band maximum energy. Holes in the valence band initiate a reaction with water, resulting in the generation of hydroxyl radicals.

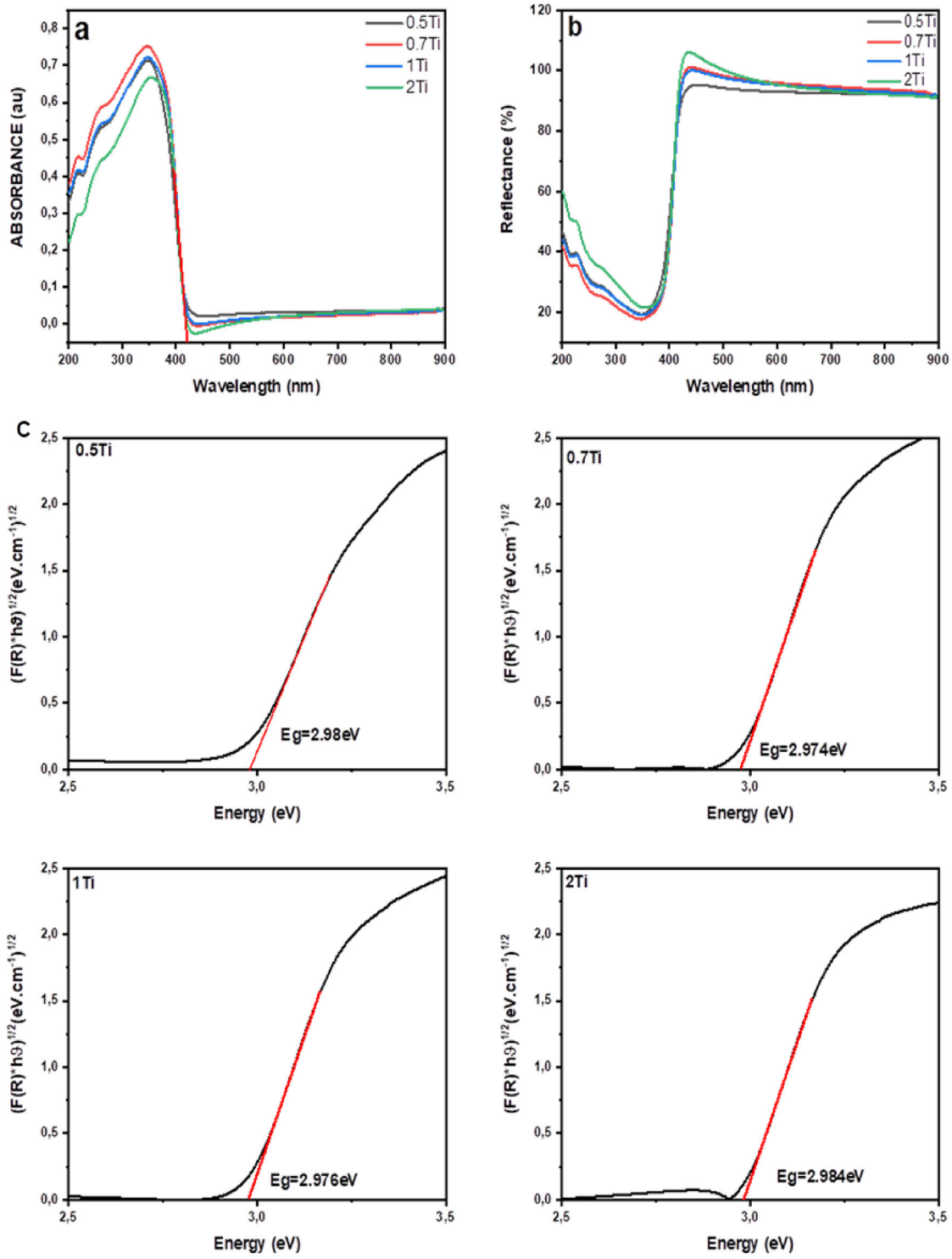

Figure 10. (a) UV—vis absorption spectra; (b) Reflectivity spectra and (c)Band-gap states of TiO_2 multiphases samples.

Simultaneously, electrons in the conduction band react with oxygen, producing superoxide anions.[95,96] This contributes to the reduction of water to produce hydrogen, Figure 14 illustrates this phenomenon.

It is worth noting that there are few works in the literature that use TiO_2 in the visible region for H_2 production, in addition, it is difficult to compare our results with those obtained in the bibliography because (i) the synthesis of the heterojunction and (ii) the operating conditions (amount of catalyst and light source) of the photocatalytic act are not the same. We still tried to make a comparison with the results of the literature. The photocatalyst $R_{52}B_{46}$ (0.7 in Ti^{+4}) has the largest hydrogen evolution

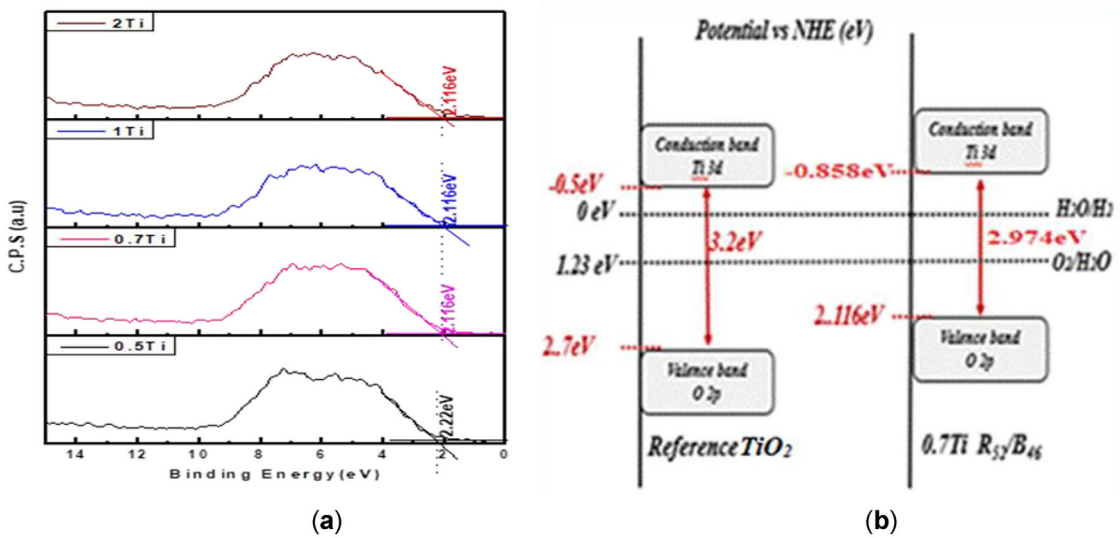

Figure 11. (a) VB XPS of TiO_2 multiphase samples; (b) Band energy diagram of reference (TiO_2),[86] and 0.7Ti sample.

Table 8. Photocatalytic activity of heterophase TiO_2 for hydrogen production.

TiO_2 Composition (%)	Amount of Catalyst	Light Source	H_2 generation Rate	Refs.
R52B46	100 mg/100 mL	LED lamps (3 × 13 W)	230 μmol g^{-1} h^{-1}	Actual study
A12R88	20 mg/80 mL	350 W Xe lamp	74,4 μmol g^{-1} h^{-1}	[62]
A74B26	20 mg/100 mL	450 W Xe lamp	101.4 μmol g^{-1} h^{-1}	[66]
A54B46	20 mg/100 mL	450 W Xe lamp	101.4 μmol g^{-1} h^{-1}	[67]

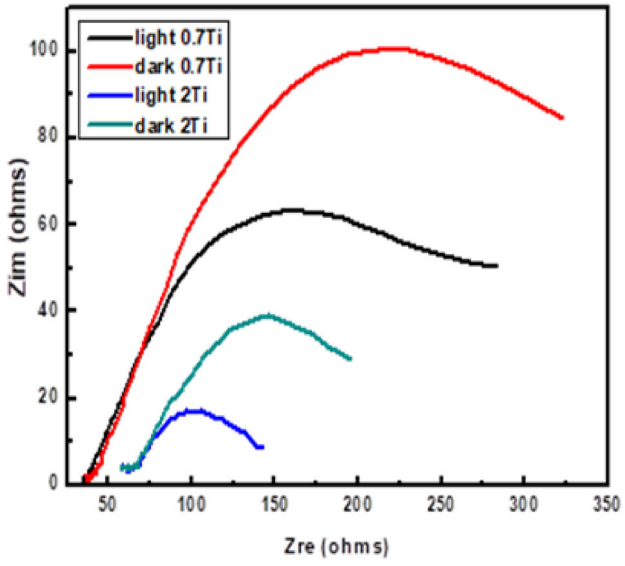

Figure 12. The EIS diagram of 0.7 and 2 Ti samples in the dark and under illumination in Na_2SO_4 (0.1 M).

rate (230 μmol h^{-1} of H_2-generation) and shows a clear enhancement in the hydrogen evolution rate compared to brookite-TiO_2 (176 mmol.h^{-1}) or rutile-TiO_2 (58 mmol.h^{-1}) as observed by Chen et. al.[56] Our results are more important compared to those obtained by Xia et al.,[62] or by Cihlar et al.[67] and are very competitive compared to those obtained by Sun et al.[68] which used TiO_2 ($R_{74}B_{24}$) prepared via hydrolysis method using dimethyl diallyl ammonium chloride and HCl. The Table 8 summarizes some examples of the performance of heterophase TiO_2 for hydrogen production.

3.6. Anatase; R: Rutile; and B: Brookite

After the photocatalytic act, both catalysts 0.7Ti (the best formulation) and 2Ti (the bad catalyst) are characterized by XRD analysis. XRD patterns are shown in Figures 15 and 16. For the 0.7T system (Figure 15), we note that the system is almost stable even after photocatalytic testing, and no change in the structure was observed. However, for the 2Ti (Figure 16) system which showed poor photocatalytic activity, a change in the structure was recorded, after photocatalysis, the system transformed almost into brookite type structure which is not active phase in H_2-production under our conditions reaction. This transformation can be explained by considering several factors related to the experimental conditions and the dynamic processes occurring during photocatalysis. Photocatalytic reactions, especially under intense light irradiation and in the presence of reactive environments (e.g., alkaline medium), can induce significant modifications to the surface properties of TiO_2. As studied by Hanaor et al.[97] surface reactions during photocatalysis can lead

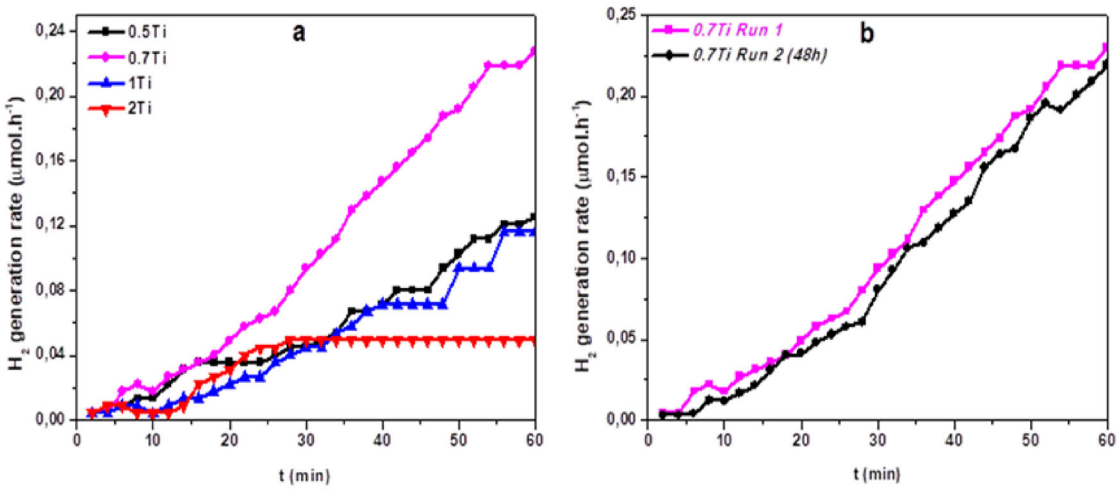

Figure 13. (a) Photocatalytic H_2 evolution rates of synthesized multiphase TiO_2, (b) cycle tests of photocatalytic H_2 evolution over 0.7Ti sample.

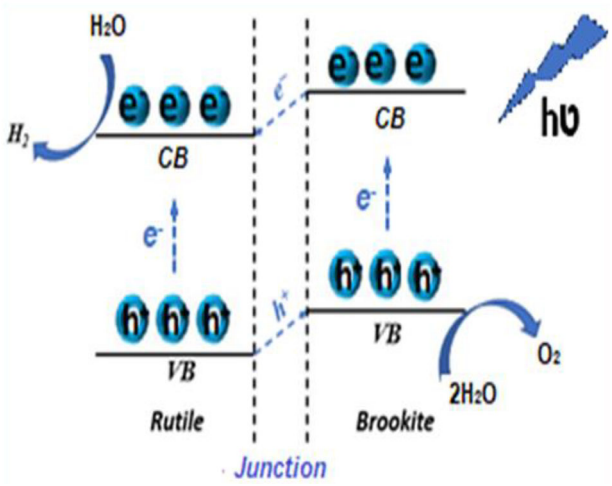

Figure 14. Schematic illustration of water splitting photocatalytic mechanism for TiO_2 heterophase rutile /brookite.

to the reorganization of the atomic structure, particularly on the nanoscale, where TiO_2 particles can be more prone to such transformations due to their high surface area (131 m^2/g in our 2Ti sample), making them sensitive to changes in phase composition. During photocatalysis, the generation of electron-hole pairs can lead to the creation or annihilation of oxygen vacancies, which play a crucial role in the stability of TiO2 phases. The literature has shown that oxygen vacancies are often located at phase boundaries (such as rutile-brookite or anatase-brookite) and can stabilize certain phases. In the case of our 2Ti sample, it is likely that the photocatalytic process caused the annihilation of these oxygen vacancies, leading to the destabilization of the rutile and halite phases and promoting the more kinetically stable brookite phase. A similar process has been observed where the loss of oxygen vacancies resulted in structural phase changes during photocatalysis.[98] The alkaline environment during photocatalysis also plays a crucial role in facilitating phase transformations. As indicated by Wang et al.[99] NaOH treatment can modify surface properties by enhancing the adsorption capacity and increasing charge separation efficiency, which leads to higher reactivity at the surface. This reactivity, combined with the loss of oxygen vacancies, could have accelerated the transformation of rutile and halite into brookite, which is more stable under the used conditions in our study.

4. Conclusions

We have successfully synthesized TiO_2 heterophases with tunable phase composition through facile hydrolysis and condensation of titanium cations method, where the initial concentration of $TiCl_4$ played as a directing factor for the structure and crystalline phases of TiO_2 (anatase/rutile/brookite). The study of the structural characteristics proved that at low concentration (0.5Ti), the proportion of heterophase junctions of the rutile and brookite phases is small and there is a high crystallization of the anatase phase. In medium (0.7 and 1 Ti) and high (2 Ti) concentrations, the crystallization rate of rutile and brookite increases, which increases the rutile/brookite heterophase junction. The sample of 0.5Ti, which presents anatase in a high proportion (79%) in its structure, has demonstrated low photocatalytic efficiency under visible light. The presence of rutile/brookite heterophase junction crossing contributes significantly to the improvement of the active sites for photocatalytic reaction and separation efficiency of photogenerated electrons and holes, which contributes to photocatalytic evolution performance under visible light for hydrogen production. The sample 0.7Ti presented the highest photocatalytic activity in H_2 production (230 µmol/h) due to the heterophase junctions R52/B46, the high pore size 20.60 nm, the almost absence of impurities and relatively small bandgap energy 2.974 eV, all this led to an improvement in the efficiency of charge separation and transfer. This work presents an easy and economical method for the synthesis of TiO_2 multi-phases that are active under visible light. We used it as a photocatalyst to produce hydrogen

Research Article
doi.org/10.1002/slct.202404396

Chemistry Europe
European Chemical Societies Publishing

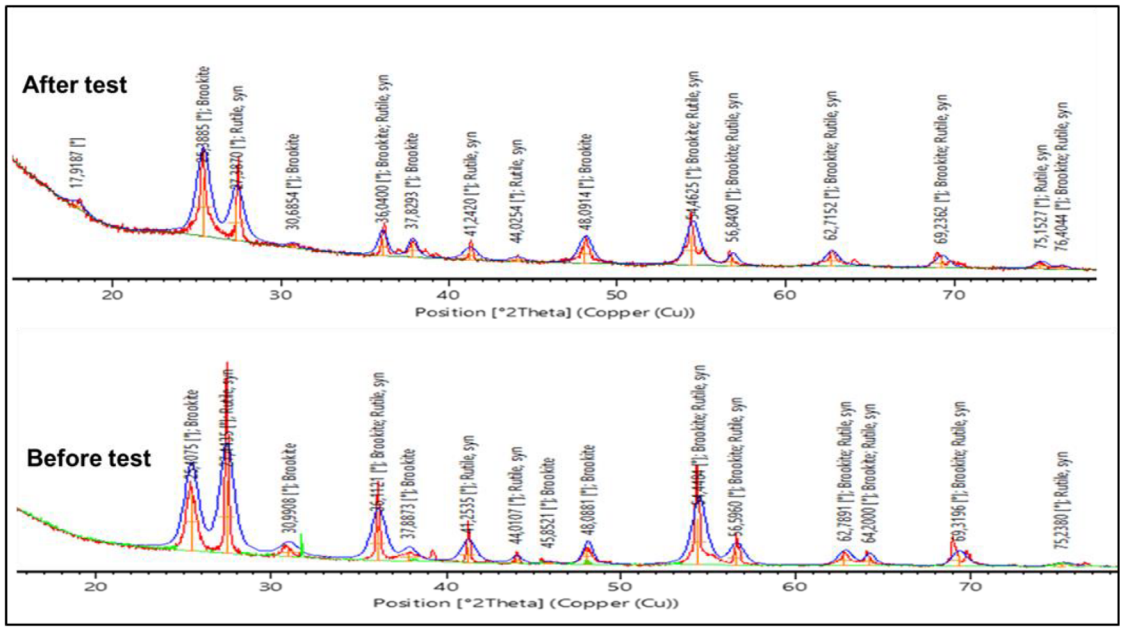

Figure 15. XRD patterns of 0.7Ti sample before and after photocatalytic reaction.

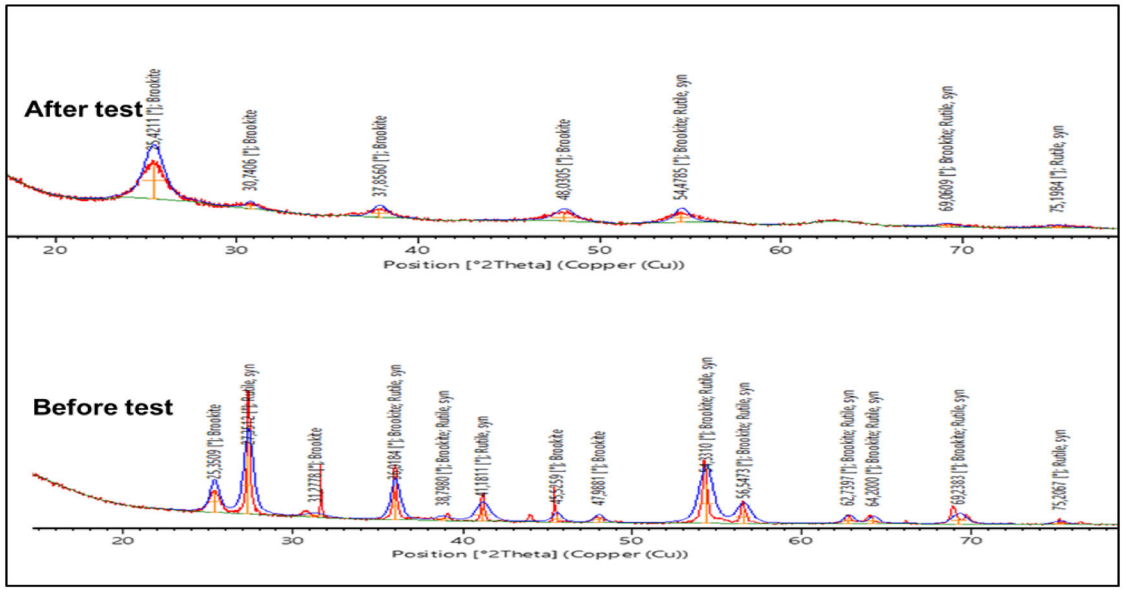

Figure 16. XRD patterns of 2Ti sample before and after photocatalytic reaction.

from the photocatalytic water-splitting reaction under visible light.

Acknowledgments

The authors have nothing to report.

Conflict of Interests

The authors declare no conflict of interests.

Data Availability Statement

The data that support the findings of this study are available from the corresponding author upon reasonable request.

Keywords: H_2 production · Heterophase junction · TiO_2 · Visible light

[1] H. Caliskan, I. Dincer, A. Hepbasli, *Int. J. Hydrogen Energy.* **2013**, *38*, 6104–6111.
[2] I. Dincer, C. Acar, *Int. J. Hydrogen Energy.* **2015**, *40*, 11094–11111.
[3] F. Yilmaz, M. T. Balta, R. Selbaş, *Renew. Sustain. Energy Rev.* **2016**, *56*, 171–178.

[4] M. Benlembarek, N. Salhi, R. Benrabaa, A. M. Djaballah, A. Boulahouache, M. Trari, *Int. J. Hydrogen Energy.* **2022**, *47*, 9239–9247.
[5] I. Dincer, *Clean: Soil, Air, Water* **2007**, *35*, 311–322.
[6] J. D. Holladay, J. Hu, D. L. King,Y. Wang, *Catal. Today.* **2009**, *139*, 244–260.
[7] S. E. Hosseini, M. A. Wahid, *Renew. Sustain. Energy Rev.* **2016**, *57*, 850–866.
[8] J. Y. Lee, W.-K. Jo, *J. Hazard. Mater.* **2016**, *314*, 22–31.
[9] T. Zhao, R. Qian, G. Zhou, Y. Wang, W. I. Lee, J. H. Pan, *Chemosphere* **2021**, *263*, 128344.
[10] M.A. Hernández-Carrillo, R. Torres-Ricárdez, M. F. García-Mendoza, E. Ramírez-Morales, L. Rojas-Blanco, L. L. Díaz-Flores, G. Pérez-Hernández, *Catal. Today.* **2020**, *349*, 191–197.
[11] H. Zhou, H. Xiong, R. Zhang, L. Zhang, L. Zhang, L. Li, Z. A. Qiao, *Small.* **2021**, *17*, 2100428.
[12] Q. Guo, C. Zhou, Z. Ma, X. Yang, *Adv. Mater.* **2019**, *31*, 1901997.
[13] K. Maeda, T. E. Mallouk, *Bull. Chem. Soc. Jpn.* **2019**, *92*, 38–54.
[14] R. Kaushik, P. K. Singh, A. Halder, *Catal. Today.* **2022**, *384*, 45–69.
[15] W. Yang, M. Li, K. Pan, L. Guo, J. Wu, Z. Li, W. Zhou, *J. Colloid Interface Sci.* **2021**, *586*, 75–83.
[16] M. A. I. Molla, M. Furukawa, I. Tateishi, H. Katsumata, T. Suzuki, S. Kaneco, *ChemEngineering* **2017**, *1*, 8.
[17] A. Rabajczyk, M. Zielecka, W. Klapsa, A. Dziechciarz, *Mate.* **2021**, *14*, 2161.
[18] P. Roy, D. Kim, K. Lee, E. Spiecker, P. Schmuki, *Nanoscale* **2010**, *2*, 45–59.
[19] V. Preethi, S. Kanmani,*Mater. Sci. Semicond. Process.* **2013**, *16*, 561–575.
[20] H. Du, Y.N. Liu, C.C. Shen, A.W. Xu,*Chin. J. Catal.* **2017**, *38*, 1295–1306.
[21] D. Chatterjee, S. Dasgupta, *J. Photochem. Photobiol. C.* **2005**, *6*, 186–205.
[22] H. K. Paumo, S. Dalhatou, L. M. Katata-Seru, B. P. Kamdem, J. O. Tijani, V. Vishwanathan, I. Bahadur, *J. Mol. Liq.* **2021**, *331*, 115458.
[23] R. Ameta, S. Benjamin, A. Ameta, S. C. Ameta, *Mater. Sci. Forum.* **2013**, *734*, 247–272.
[24] A. Kumar, P. Choudhary, A. Kumar, P. H. C. Camargo, V. Krishnan, *Small.* **2022**, *18*, 2101638.
[25] Z. Lin, Y. Zheng, F. Deng, X. Luo, J. Zou, P. Shao, H. Tang, *Sep. Purif. Technol.* **2021**, *277*, 119430.
[26] J. Luo, M. Wang, L. Chen, J. Shi, *J. Energy Chem.* **2022**, *66*, 52–60.
[27] D. Tekin, D. Birhan, H. Kiziltas, *Mater. Chem. Phys.* **2020**, *251*, 123067.
[28] G. Deo, A. M. Turek, I. E. Wachs, T. Machej, J. Haber, N. Das, A. M. Hirt, *Appl. Catal., A.* **1992**, *91*, 27–42.
[29] F. Dachille, P. Y. Simons, R. Roy, *Am. Mineral.* **1968**, *53*, 1929–1939.
[30] S. Agrawal, N. J. English, K. R. Thampi, J. M. D. MacElroy, *Phys. Chem. Chem. Phys.* **2012**, *14*, 12044–12056.
[31] M. R. Gholipour, C.-T. Dinh, F. Béland, T.-O. Do, *Nanoscale* **2015**, *7*, 8187–8208.
[32] A. A. Ismail, D. W. Bahnemann, *Sol. Energy Mater. Sol. Cells.* **2014**, *128*, 85–101.
[33] L. Díaz, V. D. Rodríguez, M. González-Rodríguez, E. Rodríguez-Castellón, M. Algarra, P. Núñez, E. Moretti, *Inorg. Chem. Front.* **2021**, *8*, 3491–3500.
[34] S. Kitano, A. Tanaka, K. Hashimoto, H. Kominami, *Appl. Catal., A.* **2016**, *521*, 202–207.
[35] M. Bowker,*Green Chem.* **2011**, *13*, 2235–2246.
[36] J. Zhang, J. A. Schott, S. M. Mahurin, S. Dai, *Small Methods* **2017**, *1*, 1600051.
[37] W. Zhang, Y. Tian, H. He, L. Xu, W. Li, D. Zhao, *Natl. Sci. Rev.* **2020**, *7*, 1702–1725.
[38] K. Maver, I. Arčon, M. Fanetti, S. Emin, M. Valant, U. L. Štangar, *Catal. Today.* **2021**, *361*, 124–129.
[39] J. Lin, T. Sun, M. Li, J. Yang, J. Shen, Z. Zhang, X. Wang, *J. Catal.* **2019**, *372*, 8–18.
[40] K. Lan, R. Wang, Q. Wei, Y. Wang, A. Hong, P. Feng, D. Zhao, *Angew. Chem.* **2020**, *132*, 17829–17836.
[41] G. Wang, T. Chen, S. Liu, F. Wang, M. Li, M. Xie, W. Han, *Dalton Trans.* **2021**, *50*, 8711–8717.
[42] M. Xu, A. Zada, R. Yan, H. Li, N. Sun, Y. Qu, *Phys. Chem. Chem. Phys.* **2020**, *22*, 4526–4532.
[43] B. K. Mutuma, G. N. Shao, W. D. Kim, H. T. Kim, *J. Colloid Interface Sci.* **2015**, *442*, 1–7.
[44] H. Tian, C. Zhang, P. Su, Z. Shen, H. Liu, G. Wang, J. Liu, *J. Energy Chem.* **2020**, *40*, 137–143.
[45] D. Yang, H. Liu, Z. Zheng, Y. Yuan, J. C. Zhao, E. R. Waclawik, H. Zhu, *J. Am. Chem. Soc.* **2009**, *131*, 17885–17893.
[46] P. Hemmati-Eslamlu, A. Habibi-Yangjeh, *FlatChem* **2023**, *43*, 100597.
[47] A. Habibi-Yangjeh, K. Pournemati, *Crit. Rev. Environ. Sci. Technol.* **2024**, *54*, 290–320.
[48] F. Seifikar, A. Habibi-Yangjeh, *Chemosphere* **2024**, *335*,141686.
[49] X. Kang, G. Dong, T. Dong, *ACS Appl. Energy Mater.* **2022**, *6*, 1025-1036.
[50] L. Ding, S. Yang, Z. Liang, X. Qian, X. Chen, H. Cui, J. Tian, *J. Colloid Interface Sci.* **2020**, *567*, 181–189.
[51] T. Berger, M. Sterrer, O. Diwald, E. Knözinger, D. Panayotov, T. L. Thompson, J. T. Yates, *J. Phys. Chem. B.* **2005**, *109*, 6061–6068.
[52] F. Cao, J. Xiong, F. Wu, Q. Liu, Z. Shi, Y. Yu, L. Li, *ACS Appl. Mater. Interfaces.* **2016**, *8*, 12239–12245.
[53] G. Tian, H. Fu, L. Jing, B. Xin, K. Pan, *J. Phys. Chem. C.* **2008**, *112*, 3083–3089.
[54] W. Li, C. Liu, Y. Zhou, Y. Bai, X. Feng, Z. Yang, K. Y. Chan, *J. Phys. Chem. C.* **2008**, *112*, 20539–20545.
[55] R. Mu, Y. Ao, T. Wu, C. Wang, P. Wang, *J. Hazard. Mater.* **2020**, *382*, 121083.
[56] J. Chen, M. Guan, X. Zhang, X. Gong, *RSC Adv.* **2019**, *9*, 36615–36620.
[57] K. Fischer, A. Gawel, D. Rosen, M. Krause, A. Abdul Latif, J. Griebel, A. Schulze, *Catalysts* **2017**, *7*, 209.
[58] Y. Y. Zaw, D. A. D. Channei, T. Threrujirapapong, W. Khanitchaidecha, A. Nakaruk, *Mater. Sci. Forum.* **2020**, *998*, 78–83.
[59] N. Wetchakun, S. Phanichphant, *Current. Appl. Phys.* **2008**, *8*, 343–346.
[60] Y. Lei, et al., *Nanomater.* **2021**, *11*, 1347.
[61] K. Yaemsunthorn, M. Kobielusz, W. Macyk, *ACS Appl. Nano Mater.* **2021**, *4*, 633–643.
[62] X. Xia, S. Peng, Y. Bao, Y. Wang, B. Lei, Z. Wang, Y. Gao, *J. Power Sources.* **2018**, *376*, 11–17.
[63] T. A. Kandiel, A. Feldhoff, L. Robben, R. Dillert, D. W. Bahnemann, *Chem. Mater.* **2010**, *22*, 2050–2060.
[64] X. Shen, B. Tian, J. Zhang, *Catal. Today.* **2013**, *201*, 151–158.
[65] Q. Tay, X. Liu, Y. Tang, Z. Jiang, T. C. Sum, Z. Chen, *J. Phys. Chem. C.* **2013**, *117*, 14973-14982.
[66] J. Cihlar, V. Kasparek, M. Kralova, K. Castkova, *Int. J. Hydrogen Energy.* **2015**, *40*, 2950–2962.
[67] J. Cihlar, L. K. T. Navarro, V. Kasparek, J. Michalicka, J. Cihlar Jr, J. Kastyl, L. Celko, *Int. J. Hydrogen Energy.* **2021**, *46*, 8578–8593.
[68] M. Sun, H. Zhou, H. Xiong, R. Zhang, Z. Liu, D. Li, Z. A. Qiao, *Catal. Today.* **2022**, *405–406*, 203–211.
[69] R. Bagtache, I. Sebai, M. Trari, *Sol. Energy.* **2020**, *211*, 971–976.
[70] O. Frank, M. Zukalova, B. Laskova, J. Kürti, J. Koltai, L. Kavan, *Phys. Chem. Chem. Phys.* **2012**, *14*, 14567–14572.
[71] M. N. Iliev, V. G. Hadjiev, A. P. Litvinchuk, *Vib. Spectrosc.* **2013**, *64*, 148–152.
[72] A. Di Paola, G. Cufalo, M. Addamo, M. Bellardita, R. Campostrini, M. Ischia, L. Palmisano, *Colloids Surf., A.* **2008**, *317*, 366–376.
[73] Y. Cao, X. Li, Z. Bian, A. Fuhr, D. Zhang, J. Zhu, *Appl. Catal., B.* **2016**, *180*, 551–558.
[74] M. G. Kim, J. E. Lee, K. S. Kim, J. M. Kang, J. H. Lee, K. H. Kim, S. G. Lee, *New J. Chem.* **2021**, *45*, 3485–3497.
[75] H. Xu, L. Zhang, *J. Phys. Chem. C.* **2009**, *113*, 1785–1790.
[76] Y. Zou, Y. Li, X. Lian, Y. Xie, X. Song, M. Wang, Z. Tian, *Appl. Phys. A.* **2020**, *126*, 618.
[77] G. A. Tompsett, G. A. Bowmaker, R. P. Cooney, J. B. Metson, K. A. Rodgers, J. M. Seakins, *J. Raman Spectrosc.* **1995**, *26*, 57–62.
[78] Y. Hu, H.-L. Tsai, C.-L. Huang, *J. Eur. Ceram. Soc.* **2003**, *23*, 691–696.
[79] X. Zhu, S. Han, W. Feng, Q. Kong, Z. Dong, C. Wang, Q. Yi, *RSC Adv.* **2018**, *8*, 14249–14257.
[80] K. S. Sing, *Pure Appl. Chem.* **1985**, *57*, 603–619.
[81] L. P. Lekesi, T. E. Motaung, S. V. Motloung, L. F. Koao, T. D. Malevu, *J. Mol. Struct.* **2022**, *1251*, 132014.
[82] Z. Fan, F. Meng, J. Gong, H. Li, Z. Ding, B. Ding, *J. Mater. Sci.: Mater. Electron.* **2016**, *27*, 11866–11872.
[83] R. Shvab, E. Hryha, L. Nyborg, *Powder Metall.* **2017**, *60*, 42–48.
[84] R. Nawaz, C.F Kait, H. Y. Chia, M. H. Isa, L. W. Huei, *Nanomater* **2019**, *9*, 11.
[85] L. Li, J. Yan, T. Wang, Z. J. Zhao, J. Zhang, J. Gong, N. Guan, *Nat. Commun.* **2015**, *6*, 5881.
[86] Y. Luo, X. Feng, Z. Chen, X. Shen, *Mater. Adv.* **2022**, *3*, 8830–8847.
[87] H. A. Foster, I. B. Ditta, S. Varghese, A. Steele, *Appl. Microbiol. Biotechnol.* **2011**, *90*, 1847-1868.

[88] N. Venkatachalam, M. Palanichamy, B. Arabindoo, V. Murugesan, *J. Mol. Catal. A: Chem.* **2007**, *1*, 158–165.
[89] D. R. Eddy, et al., *Nanomater.* **2023**, *13*, 704.
[90] C. Zhang, Y. Li, D. Shuai, Y. Shen, D. Wang, *Chem. Eng. J.* **2019**, *355*, 399–415.
[91] A. Bahdaouia, S. Amara, L. Adnane, S. Columbus, K. Daoudi, A. Mahieddine, *Int. J. Hydrogen Energy.* **2022**, *47*, 9301–9318.
[92] S. Bagheri, N. M. Julkapli, *Rev. Inorg. Chem.* **2017**, *37*, 11–28.
[93] A. Franciosi, C. G. Van de Walle, *Surf. Sci. Rep.* **1996**, *25*, 1–140.
[94] R. T. Tung, L. Kronik, *Adv. Theory Simul.* **2018**, *1*, 1700001.
[95] M. K. Singh, M. S. Mehata, *Opt.* **2019**, *193*, 163011.
[96] T. Sato, M. Taya, *Biochem. Eng. J.* **2006**, *28*, 303–308.
[97] D. A. H. Hanaor, C. C. Sorrell, *J. of Mat. Sci.* **2011**, *46*, 855–874.
[98] G. Colón, M. C. Hidalgo, G. Munuera, I. Ferino, M. G. Cutrufello, J. A. Navío, *App.Catal. B: Envi.* **2006**, *63*, 45–59.
[99] Q. Wang, et al., *J. of Mat. Chem A.* **2019**, *7*, 14613–14619.

Manuscript received: September 17, 2024